JGR Oceans

RESEARCH ARTICLE
10.1029/2019JC016033

Key Points:
- The WCR formation from the GS has almost doubled from 1980–1999 to 2000–2017 with a significant upward regime shift in the GS behavior
- The average lifespan decreased from Regime 1 to Regime 2; while the size remained invariant
- The overall impact of increasing WCR on the slope is estimated to be about 80% between 75°W and 65°W and 25–60% to the east of 65°W

Supporting Information:
- Supporting Information S1
- Video S1

Correspondence to:
A. Gangopadhyay,
avijit.gangopadhyay@umassd.edu

Citation:
Gangopadhyay, A., Gawarkiewicz, G., Silva, E. N. S., Silver, A. M., Monim, M., & Clark, J. (2020). A census of the warm-core rings of the Gulf Stream: 1980–2017. *Journal of Geophysical Research: Oceans*, *125*, e2019JC016033. https://doi.org/10.1029/2019JC016033

Received 31 DEC 2019
Accepted 18 JUN 2020
Accepted article online 29 JUN 2020

A Census of the Warm-Core Rings of the Gulf Stream: 1980–2017

Avijit Gangopadhyay[1], Glen Gawarkiewicz[2], E. Nishchitha S. Silva[1], Adrienne M. Silver[1], M. Monim[3], and Jenifer Clark[4]

[1]School for Marine Science and Technology, University of Massachusetts Dartmouth, Dartmouth, MA, USA, [2]Woods Hole Oceanographic Institution, Woods Hole, MA, USA, [3]RPS Group, South Kingstown, RI, USA, [4]Jenifer Clark's Gulfstream, Dunkirk, MD, USA

Abstract A census of Gulf Stream (GS) warm-core rings (WCRs) is presented based on 38 years (1980–2017) of data. The census documents formation and demise times and locations, and formation size for all 961 WCRs formed in the study period that live for a week or more. A clear regime shift was observed around the Year 2000 and was reported by a subset of authors (Gangopadhyay et al., 2019, https://doi.org/10.1038/s41598-019-48661-9). The WCR formation over the whole region (75–55°W) increased from an average of 18 per year during Regime 1 (1980–1999) to 33 per year during Regime 2 (2000–2017). For geographic analysis formation locations were grouped in four 5° zones between 75°W and 55°W. Seasonally, WCR formations show a significant summer maxima and winter minima, a pattern that is consistent through all zones and both temporal regimes. The lifespan and size distribution show progressively more rings with higher longevity and greater size when formed to the east of 70°W. The average lifespan of the WCRs in all four zones decreased by 20–40% depending on zones and/or seasons from Regime 1 to Regime 2, while the size distribution remained unchanged across regimes. The ring footprint index, a first-order signature of impact of the WCRs on the slope, increased significantly (26–90%) for all zones from Regime 1 to Regime 2, with the highest percent increase in Zone 2 (70–65°W). This observational study establishes critical statistical and dynamical benchmarks for validating numerical models and highlights the need for further dynamical understanding of the GS-ring formation processes.

1. Introduction

One of the major drivers of the changes in the shelf and slope waters off the coasts of the northeast United States and southeastern Canada is thought to be the latitudinal excursions of the Gulf Stream (GS) bringing warm waters into the slope sea in the form of multiple warm-core rings (WCRs) and streamers/shingles from the GS. Determining the impact of the WCRs on the shelf-slope exchange and thus on the water masses on the shelf (Bisagni, 1983; Gawarkiewicz et al., 2001; Joyce & McDougall, 1992; Ramp et al., 1983) is one of the priorities of the Ocean Observatories Initiative (OOI) science plan for the Pioneer Array (Gawarkiewicz & Plueddemann, 2020) and has been a major area of active research (e.g., Chaudhuri, Bisagni, et al., 2009; Chaudhuri, Gangopadhyay, et al., 2009; Chen et al., 2014; Gawarkiewicz et al., 2018; Gangopadhyay et al., 2019; Zhang & Gawarkiewicz, 2015). The frequent occurrence and impact of WCRs on the physical, chemical, and biological oceanography of the slope sea area have been documented in the past through field observations (Joyce, 1985; Lai & Richardson, 1977; Saunders, 1971), satellite imagery (Auer, 1987; Bisagni, 1976; Brown et al., 1986; Halliwell & Mooers, 1979), and theoretical models (Csanady, 1979; Flierl, 1977; Olson et al., 1985). A systematic study of WCR formation and distribution is a critical need to understand the impact of changing ring frequency and characteristics on the underlying ecosystem and its habitats.

Previous climatological studies were limited by the number of years of data availability. For example, Cerone (1984) identified typical ring formation patterns based on sparsely available synoptic temperature charts over the period 1976 to 1981. Joyce (1985) and references therein reported on individual ring structures (and their changes in volume, energetics and momentum) for a collection of WCRs from data collected during a targeted survey during 1981–1982. Auer (1987) developed a 5-year climatology of the GS and its WCRs based on data from 1982–1986. Myers and Drinkwater (1986) used data from 1980 to 1984 to explore possible relationships between six groundfish stocks and WCR occurrences. They extended their study later

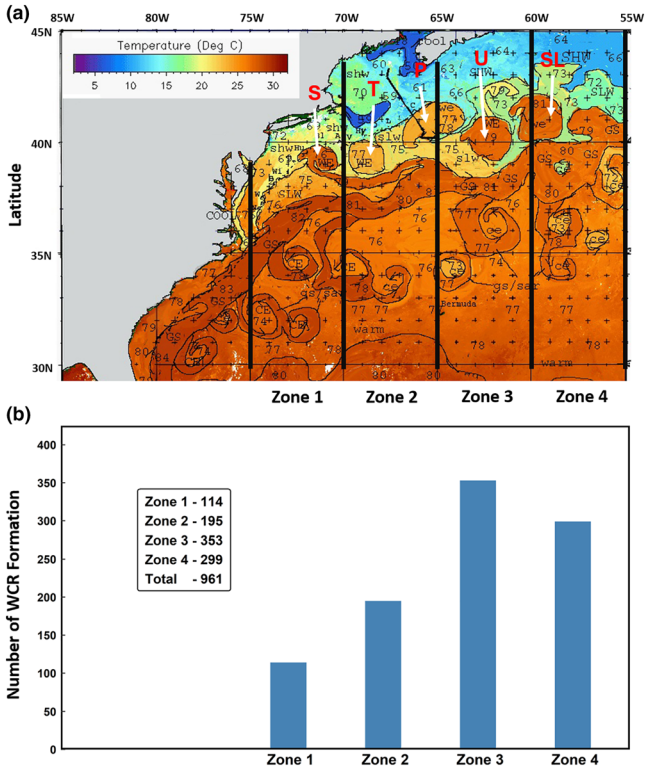

Figure 1. (a) Zones on a typical chart of 2 August 2017. Four WCRs (S, T, P, and U) are seen in this chart with another short-lived (lifespan < 7 days) ring SL. (b) Number of WCR formations in different zones. The zones are as follows. Zone 1: 75–70°W, Zone 2: 70–65°W, Zone 3: 65–60°W, and Zone 4: 60–55°W (figure modified from Gangopadhyay et al., 2019).

to establish a negative correlation between 17 groundfish stocks and WCRs based on data from 1973 to 1986 (Myers & Drinkwater, 1989).

We now have access to a consistent 38-year-long (1980–2017) data set documenting the occurrence and pathways of the WCRs in the GS area (75–55°W) on a semiweekly basis. Some aspects of the seasonal and interannual variability of WCR formation along the GS path from 75°W to 55°W was recently discussed by Gangopadhyay et al. (2019). They identified a regime shift around 2000 in the WCR formation (Figure 2a). Out of a total of 961 WCRs formed during1980–2017, 360 WCRs were formed during Regime 1 (1980–1999) with an average of 18 rings annually, and 601 WCRs were formed during Regime 2 (2000–2017), with an average of 33 rings annually.

In this study, we extend the previous study in order to present further detailed geographical statistics of ring formation as well as lifespan and size distributions. The overall area of 75–55°W was subdivided into four distinct zones (Zone 1: 75–70°W, Zone 2: 70–65°W, Zone 3: 65–60°W, and Zone 4: 60–55°W). The rationale for subdividing the overall 2,000-km span of the GS stems from two factors. First, the GS is shown to be responding with different temporal (on both interannual and secular time scales) variability east and west of 65–60°W (Zone 3), also called the transition zone (Bisagni et al., 2017; Gangopadhyay et al., 2016). Second, further geographic perspective provides more information on Ring formation dynamics for two reasons: (i) Zone 1 (75–70°W) is generally a standing meander pattern for the GS with less ring activity and (ii) the New England Seamount Chain (NESC) underlies the GS between 65°W and 60°W (Zone 3), thus creating large-amplitude meanders after 65°W with frequent WCR formation to the east. Our specific objectives are to (i) briefly describe the seasonal to interannual variability including the regime shift around the Year 2000, (ii) determine the spatial variation of the size and lifespan distribution of the WCRs, and (iii) investigate the changes in the lifespan and size distribution of the rings formed from one temporal regime to the other.

The organization of this paper is as follows. Section 2 outlines the data sets used to create the census and the methodology to analyze the WCR characteristics. Section 3 presents seasonal and interannual variability (including the regime shift) within the four zones. Three aspects of the WCRs, namely, the seasonality, lifespan, and size characteristics for the two regimes, are highlighted in this section as well. Section 4 discusses the major results and outlines possible dynamical factors behind the observed differences in WCR characteristics for the two different regimes. Section 5 summarizes the results with some concluding remarks about future implications and research directions from this study.

2. Data and Methods

The main data set that was used is a set of charts prepared by one of the coauthors, Jenifer Clark (an example chart for 2 August 2017 is shown in Figure 1a). We have access to this unique collection of charts of the GS and surrounding waters that have been annotated with satellite data indicating temperature. Using infrared imagery and surface in situ temperature data, oceanographic analyses were produced for this area in the form of synoptic charts two to three times a week in a consistent manner. These charts show the location, extent, and temperature signature of currents (GS and shelf break front), warm- and cold-core rings (WCRs and CCRs), other eddies, shingles, intrusions, and other water masses in the Gulf of Maine (GOM), over Georges Bank (GB), and in the Mid-Atlantic Bight (MAB). National Oceanic and Atmospheric Administration (NOAA) produced and used these charts during 1980–1995 and analyzed them for GS front extraction. These charts were also used for WCR identification and tracking by the Bedford Institute of Oceanography (BIO), utilized for operational application by the U.S. Navy and regularly used

by fishermen, sailors, numerical ocean modelers, oil and gas geologists, and weather forecasters. This set of charts is indeed the most consistent data set that has documented the signatures of the GS and its rings for the last four decades. An animation with all available annotated charts for 2017 is available in supporting information (Supporting Information Video S1).

These charts have been used in the past by various researchers for different purposes. Cerone (1984), Brown et al. (1986), and Auer (1987) used these charts over different 5-year periods in the 1980s to develop WCR climatology and related statistics. Robinson et al. (1988) used these charts to predict for the first time CCR propagation and their acoustic propagation effects for the U.S. Navy. Such charts were used recently for interannual variability studies (Chaudhuri, Bisagni, & Gangopadhyay, 2009, Chaudhuri, Gangopadhyay, & Bisagni, 2009) and for Integrated Ocean Observation System (IOOS)-related operational forecasting (Gangopadhyay et al., 2013; Schmidt & Gangopadhyay, 2013; Schofield et al., 2010).

JC charts are available two to three times a week during 1980–2017. Thus, approximately 5,000 charts were used for the 38 years of analysis. The analysis domain for the charts extended often to 45°W during 1980 to 1996 while being restricted to 55°W during 1997 to 2017. A substantive period (1980–2004) was analyzed by Roger Pettipas at BIO for WCR formation and tracking. Part of the BIO data set (1980–1999) was used by Chaudhuri, Gangopadhyay, and Bisagni (2009) for identifying all WCRs born from the GS up to 45°W. Chaudhuri, Gangopadhyay, and Bisagni (2009) also validated these data for extracting WCR numbers with available sea surface temperature (SST) and sea surface height (SSH) maps.

For the purpose of creating a consistent chart data set to extract the WCR formation statistics for the 38-year period, the 2,000-km domain from 75°W to 55°W was chosen as the study area for all charts. Then a three-step method was followed: (i) The WCR information from the BIO ring tracking information until 45°W was filtered to extract all the ring formation west of 55°W, (ii) the charts from 1997 to 2017 have been analyzed by coauthors Monim (2017) and Silva (2019) using the QGIS Version 2.18.16 product (QGIS Development Team, 2016), and (iii) a validation of the BIO and Monim (2017) analysis was carried out for a common 8-year period (1997–2004) to establish confidence and continuity in WCR identification between analysts.

While the first step is self-explanatory, the second and third steps need elaboration. All the JC charts (1997–2017) were first georeferenced (Hackeloeer et al., 2014) using the Georeferencer tool in the QGIS. Then these were added to a GIS data frame. The analyst examines each chart on a GIS framework and follows the set of rules (formation, continuity, and dissipation) to identify all WCRs on each chart and digitizes on the WGS84 coordinate system (Decker, 1986). A new ring formation is documented in the following situations: (i) a typical GS crest forming a closed anticyclonic vortex and detaches from the stream in the slope water, (ii) an anticyclonic eddy forms off of another large anticyclonic eddy in the slope water, (iii) an anticyclonic eddy further away from the stream coming into the domain through Region 4 (Monim, 2017). Note that any anticyclonic eddy that existed for less than 7 days was not counted in the census (Silva, 2019).

For each newly formed WCR, its center position (latitude/longitude) and initial area was calculated using the field calculator (QGIS Project, 2016) to two significant digits. For each WCR being dissipated, its last seen location center position was marked. The primary parameters (date of formation, center location at formation, ring outline, and last date of sighting) are stored in the GIS database. The database was exported as the final annual WCR census. An example census for part of the Year 2017 is shown in Table 1, overlapping the time of the chart in Figure 1a. The evolution of the GS is evident leading to the formation and subsequent demise of the WCRs (S, T, P and U in Figure 1a) from the chart animation provided in Supporting Information Video S1. Note that the short-lived (SL) ring in Figure 1a is not included in the census as its lifespan was less than 7 days.

There was a period for 6 months during October 1995 to March 1996, when there was a break in the JC charts (and in the BIO analysis). We had revisited the Altimetric data during this time and found six more WCRs (three during October-November-December of 1994 and three during January-February-March of 1995), which are present in our new census. All of the available BIO analysis (1980–2004) and the Monim (2017) census (1997–2016) had been revalidated against the charts, and we have followed the naming convention of Monim (2017) to identify the WCRs as shown in an example census for 2017 (Table 1). The error in the location of the WCR center and size is about 2 km or less, which has been determined based on

Table 1
An Example WCR Census From 2017 (Partial), Where DOB Is Date of Birth and DOA Is Date of Absorption

2017 WCR census							
WCR name	DOB	Longitude_F	Latitude_F	Area (km^2)	DOA	Longitude_D	Latitude_D
WE20170116E	2017-01-16	−63.98	41.62	32,064	2017-04-19	−64.65	41.26
WE20170130F	2017-01-30	−68.21	39.44	14,079	2017-05-03	−73.49	38.07
WE20170329G	2017-03-29	−56.82	41.29	13,243	2017-04-28	−59.46	41.09
WE20170329H	2017-03-29	−68.04	38.69	10,749	2017-05-15	−69.77	38.93
WE20170419I	2017-04-19	−61.46	40.45	37,389	2017-06-16	−64.25	41.55
WE20170419J	2017-04-19	−64.37	40.2	24,635	2017-05-22	−64.8	40.23
WE20170421K	2017-04-21	−71.25	38.77	9,685	2017-05-03	−70.99	38.85
WE20170503L	2017-05-03	−73.92	37.25	4,418	2017-05-12	−73.8	37.17
WE20170512M	2017-05-12	−71.32	38.81	7,803	2017-05-22	−71.25	38.8
WE20170517N	2017-05-17	−56.82	40.7	43,615	2017-06-09	−57.59	40.91
WE20170522O	2017-05-22	−74.26	36.78	4,191	2017-06-09	−74.28	36.53
WE20170529P	2017-05-29	−61.05	40.31	35,638	2017-09-13	−65.86	40.22
WE20170605Q	2017-06-05	−69.52	39.67	7,448	2017-06-26	−69.76	39.67
WE20170605R	2017-06-05	−71.47	39.01	5,424	2017-07-03	−71.59	39.21
WE20170605S	2017-06-05	−67.24	39.82	11,022	2017-09-04	−71.63	38.41
WE20170707T	2017-07-07	−66.82	39.62	19,183	2017-12-13	−74.2	36.6
WE20170712U	2017-07-12	−59.74	42.12	70,213	2017-08-02	−60.86	41.97
WE20170712V	2017-07-12	−61.88	40.45	35,636	2017-08-04	−62.26	40.2
WE20170804W	2017-08-04	−56.29	40.97	18,679	2017-08-14	−56.25	40.95
WE20170809X	2017-08-09	−61.31	41.45	34,282	2017-08-28	−61.56	41.39
WE20170811Y	2017-08-11	−59.17	42.02	42,119	2017-10-30	−63.04	41.04
WE20170828Z	2017-08-21	−57.21	42.24	18,856	2017-09-04	−57.19	42.23
WE20170828a	2017-08-28	−62.77	41.87	39,489	2017-10-23	−63.73	42.07
WE20170904b	2017-09-04	−72.67	37.73	6,753	2017-09-29	−72.61	38.02
WE20170906c	2017-09-06	−57.68	42.56	23,429	2017-09-15	−57.56	42.46

Note. Coordinates with "F" are formation coordinates and coordinates with "D" represents the set of last seen (demise) coordinates. The complete census of all years (1980–2017) is available online (at https://www.bco-dmo.org/dataset/810182). Dates are formatted as YYYY-MM-DD.

digitization errors of the GIS procedure. These errors have a negligible effect on the statistics presented in this study where the results are presented for 5° wide zones.

We have compared 8 years (1997–2004) of WCR tracking records from BIO database against the recent analysis (Monim, 2017) in the area 75°W to 55°W. The mean of the annual WCR formation differences (from 8 years of data) between the two independent analyst estimates is 1.1 rings and the standard error is 1.2 rings. The BIO database is generated using the Jenifer Clarks charts, and thus, the difference is mostly due to subjective judgment of the analyst and in their interpretation of which eddy to consider as a new eddy in case of a ring-ring interaction and a formation after a ring-meander interaction. This WCR data set is thus a first comprehensive set of WCR information that is compatible with previous studies and verified by SST and SSH data for the past 38 years.

Thirty-eight years of WCR census yielded 961 WCRs, and their dates of formation, dissipation, center positions, radii (size/area), and lifespan were documented. The complete census is available at https://www.bco-dmo.org/dataset/810182 (Gangopadhyay & Gawarkiewicz, 2020). Analysis was carried out for the full area (75–55°W) and for four zones (75–70°W, 70–65°W, 65–60°W, and 60–55°W) shown in Figure 1a. The majority of the WCRs were born east of 65°W, with more births in Zones 3 and 4 (Figure 1b). This is consistent with previous studies (Cornillon, 1986; Lee & Cornillon, 1996) showing that GS meander amplitude increases across the NESC due to unstable meandering of the GS. Out of a total of 961 WCRs formed, Zone 1 had 12% (114) and Zone 2 about 20% (195) of the rings. The more productive areas to the east had 37% (353) and 31% (299) for Zones 3 and 4, respectively (see Figure 1b). Note that a few rings enter the domain in Zone 4, which are formed east of 55°W; however, their number is less than 10% of the rings in Zone 4. To summarize the geographic pattern of WCR formation, more than two thirds (~68%) of the WCRs were formed to the east of 65°W, or the NESC.

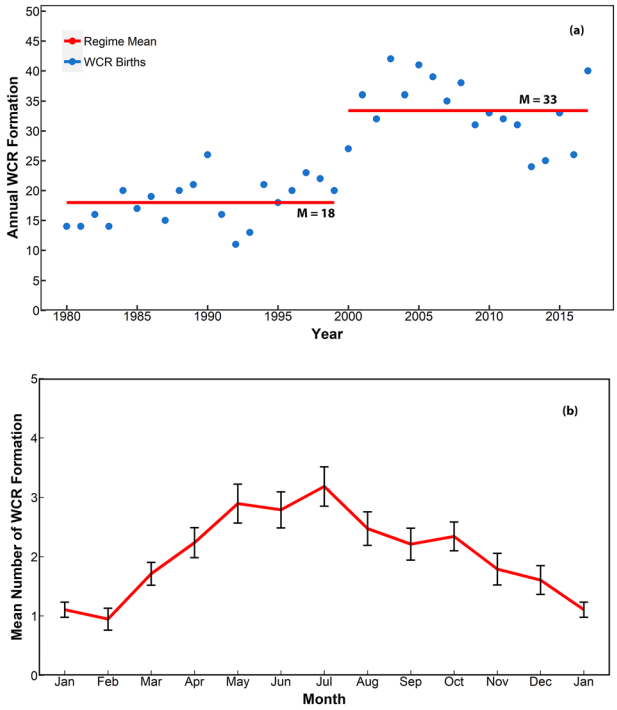

Figure 2. (a) Interannual variability of the WCR formation between 1980 and 2017 for the whole area 75–55°W. The regime shift (denoted by the split in the red solid line) is significant at the turn of the century. "M" is the mean for the regime. (b) Seasonal cycle of WCR formation over the whole area between 75°W and 55°W. The vertical bars denote the standard error of mean for each month (figure adapted from Gangopadhyay et al., 2019).

A sequential regime shift detection algorithm based on examining mean and variance (Rodionov, 2004, 2006; Rodionov & Overland, 2005) was used to identify possible regime shifts. In addition, the Markov regime switch models (Hamilton & Susmel, 1994; Kim & Nelson, 1999; Perlin, 2014) were also used to detect the regime shifts and yielded the same result of a shift around 2000. See Gangopadhyay et al. (2019) for details.

Using the census data, we developed a WCR footprint index (RFI) to understand the area of WCR presence in the slope waters during the two different temporal regimes. We first calculated the average propagation speed of every WCR using the distance between formation and final locations. Based on the average propagation speed, we determined the time spent by a WCR in each zone. The footprint of a ring was then obtained by integrating the area covered by the WCR from Time t1 to t2 (time spent in a specific zone) as follows:

$$\text{Footprint of a WCR} = \int_{t_1}^{t_2} \pi \left(R_b e^{\left(\frac{-t}{a}\right)} \right)^2 dt = \frac{\pi R_b^2}{2} a \left[e^{\left(\frac{-2t_1}{a}\right)} - e^{\left(\frac{-2t_2}{a}\right)} \right] \quad (1)$$

where R_b is the equivalent radius of the WCR at birth, a is the expected lifespan (which depends on its formation zone and season) of the WCR, t_1 is the age when the WCR entered the specific zone, and t_2 is the age when the WCR left that zone. Here we assumed WCR size decay was exponential (following Brown et al., 1986) where the equivalent radius of a WCR at a time t is given by $R_b e^{(-t/a)}$. See section 4.5 for detail quantification of the expected lifespan (a).

The size-based presence was then summed up for each zone and regime to yield the total WCR footprint during both regimes for each zone. To normalize the time period of this presence, and to generate a RFI for a zone, the WCR footprint was divided by the time period of the regime and area of the slope sea in each zone as follows.

$$WCR\ Footprint\ Index\ (RFI)|_z = \frac{\sum_R (WCR\ Footprint)_z}{(Regime\ time\ period \times Slope\ area\ in\ the\ zone)} \quad (2)$$

3. Results

In this section, the results from the regime-shift analysis (Gangopadhyay et al., 2019) are summarized first. Next, we investigate three particular characteristics of the WCR behavior from the formation census: seasonality, lifespan, and size distributions of the WCRs in the two regimes and over the four 5° zones. For each of the three characteristics, the results are described first over the whole time period within the whole domain (75–55°W), then for each of the zones, and then over the two regimes (1980–1999 and 2000–2017) for each of the four zones. The formation numbers, lifespan, and size distributions in different zones in the two regimes gives a more complete picture of the complex behavior of the large-scale GS in each of the two temporal regimes.

3.1. Regime Shift

For details on the method and results of the regime-shift analysis, please see Gangopadhyay et al. (2019). A significant regime shift around 1998–2000 is detected in WCR formation for each of the individual zones. (See Figure 2 of Gangopadhyay et al., 2019.) This pervasive nature of the regime shift across all the four zones was clearly demonstrated in the analysis metrics presented in Table 2 of Gangopadhyay et al. (2019). The average annual zone-wise increase from Regime 1 to Regime 2 is 1 to 4, 3 to 7, 7 to 12, and 6 to 10 for

Table 2
A Comparison of WCR Mean Lifespan for different periods from this study and from Brown et al. (1986) study (B86)

Lifespan characteristic	Mean from this study	Mean from B86	Median from this study
1980–1983	101	130	63 (81*)
1980–1989	90	N/A	56
Regime 1 (1980–1999)	79		53
Regime 2 (2000–2017)	60	N/A	38
1980–2017	67	N/A	42
1980–2017 (ring life <150 days)	47	54	
1980–2017 (ring life >150 days)	217	229	

*median from B86 study.

Zones 1, 2, 3, and 4, respectively (Figures 2b–2e). All of the individual methods mentioned in section 2 for detecting the regime change (Hamilton & Susmel, 1994; Perlin, 2014; Rodionov, 2006) unequivocally supported the upward shift around 2000 for all of the zones and the whole region from 75°W to 55°W.

3.2. Seasonality

On a seasonal scale, we find that WCR formation peaks in late spring/early summer (June-July-August) while the wintertime (January–February) has fewer ring formations (Figure 3a), a pattern that has been noted in the previous literature (Kang et al., 2016; Robinson et al., 1988; Stammer, 1998; Zhai et al., 2008).

The seasonal cycle for each zone is shown in (Figures 3a–3d). The vertical bars show the standard errors. For each of the zones, the WCR formation numbers go up during late spring and early summer. However, there are noticeable differences among the zones. For example, Zone 1 is mostly active in May; Zone 2 is active during April through November at a similar activity level. Zone 3 is more active than Zones 1 and 2 throughout the year, and its activity rate is about one ring per month during May through August. Zone 4 is slightly more active than Zone 3 during March. Such distributed peaking of ring activity resulted (cumulatively) in the overall spring-summer peaking in the seasonal picture for the whole area (Figure 3a).

For the whole area, the number of WCR formations has considerably increased during all seasons from Regime 1 to Regime 2. Specifically, the increase was almost 74% during summer, peaking to 87% during fall, increased by 43% during winter, and by 55% in spring.

The seasonal cycles of ring formation for the whole area and for each zone are very similar in each regime to that presented for the whole 38-year period as presented in Figures 3a–3d. There is a clear indication of an increase in WCR formation events over all seasons during Regime 2 compared to Regime 1. The formation of WCRs has increased by almost 50% in Zones 2, 3, and 4 from Regime 1 to Regime 2. In Zone 1, the rate of formation increased substantially by three to six times for spring, summer, and fall in Regime 2 relative to the earlier regime. See section 4.2 later.

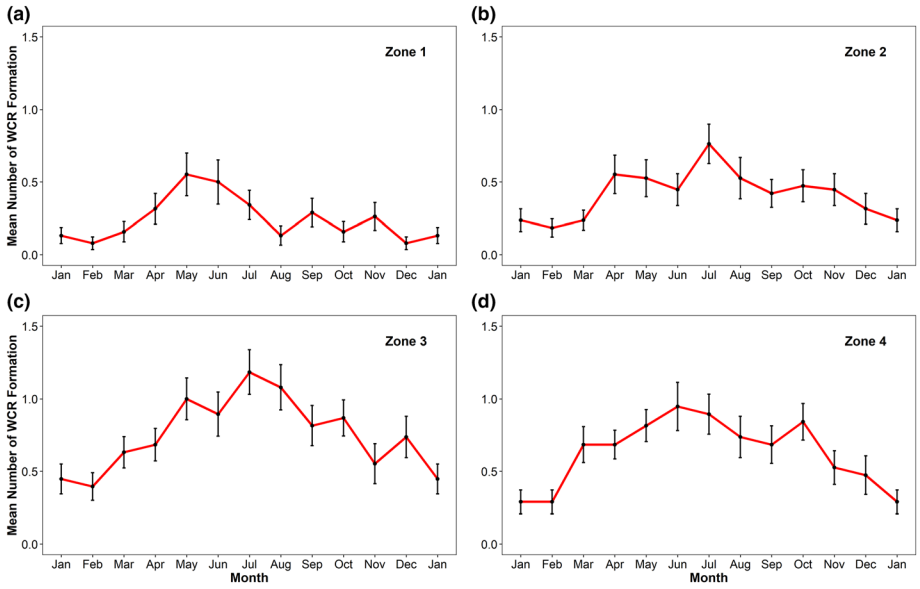

Figure 3. Seasonal cycle of WCR formation in each of the four zones from the census of 1980–2017. The vertical bars denote the standard error of mean for each month. The zones are as follows. (a) Zone 1: 75–70°W, (b) Zone 2: 70–65°W, (c) Zone 3: 65–60°W, and (d) Zone 4: 60–55°W.

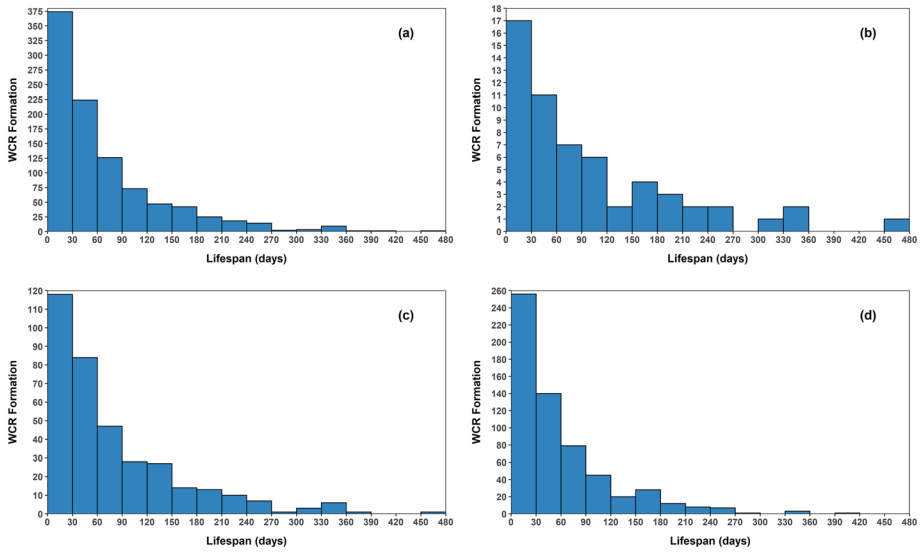

Figure 4. Lifespan distribution of WCR formations for different periods. (a) Full period (1980–2017) shows a clear exponential distribution with an *e*-folding scale of about 60 days. (b) Period 1980–1983. The apparent bimodality agrees with the results of B86 study. (c) Regime 1 (1980–1999) distribution similar to the full period's distribution in (a). (d) Regime 2 (2000–2017) distribution is similar to the full period with a hint of bimodality around Day 140. The distributions in (b)–(d) have *e*-folding scales of around 60–80 days.

3.3. Lifespan Characteristics

Figure 4 presents the lifespan distribution of the WCRs for the different periods: (i) the whole period, (ii) the common period with the Brown et al. (1986) (hereafter, B86) study, (iii) for Regime 1, and (iv) for Regime 2. The distributions show an exponential shape with formation numbers *e*-folding (reduced to e^{-1}) by around 60 days for the whole period (1980–2017), by about 80 days for Regime 1 and by 60–70 days for Regime 2. This distribution is different than the bimodal distribution obtained by B86 based on a 10-year study between 1974 and 1983. When the present census data was subset to the 1980–1983 period, this bimodality was also visible (Figure 4b). A hint of bimodality is present in the second regime (Figure 4d) but was missing in the first regime (Figure 4c). The causes and consequences of this bimodality need further investigation.

The mean lifespan of the WCRs has gradually decreased from 101 days (during 1980–1983) to 90 days (1980–1989) to 79 days (1980–1999) and to 60 days (during 2000–2017). The overall mean lifespan for the whole period (1980–2017) was obtained as 67 days compared to the mean lifespan of 120 days during 1974–1983 (B86). These are listed in Table 2. When the WCR population was divided into two lifespan groups (younger or older than 150 days, similar to B86), the mean lifespan was determined to be 47 (217) days for the SL (long-lived) group, which were a bit less than the B86 study, who found 54 and 224 days, respectively. Figure 5 presents the locations of formation for these two types of rings. Clearly, the long-lived rings were formed east of 68°W, agreeing with other studies (B86; Joyce & Wiebe, 1983, Richardson, 1983). Figure 5b presents the corresponding demise locations of all of the WCRs in this census grouped similarly. The long-term WCRs tend to follow the shelf break southwestward after encountering steep bathymetry. This creates a hot spot (71°W, 40°N to 75°W, 36°N) of ring-shelf interaction. This phenomenon will be discussed later in section 4.

To investigate how the lifespans of the WCRs vary by their formation longitude, all the WCRs have been divided into seven lifespan groups: six 30-day equal bins and one bin >180 days. Each of the lifespan groups was then divided into the four separate 5° zones. The zone-specific distribution of WCR lifespan groups for the whole period (1980–2017) is presented in Figure 6a. For the 38-year period, the WCRs from the first three lifespan groups (1–30, 31–60, and 61–90 days) are greater in numbers on the east side of 65°W than to the west. The next lifespan group (91–120 days) is least abundant in the 75–70°W area (Figure 6a). Zones 2, 3, and 4 produced more WCRs from the long-lived group (≥120 days) then Zone 1, with only one ring from this lifespan group forming in Zone 1. When similar lifespan groups are compared across regimes (Figures 6b and 6c) the increased number of SL WCRs is apparent across all of the zones.

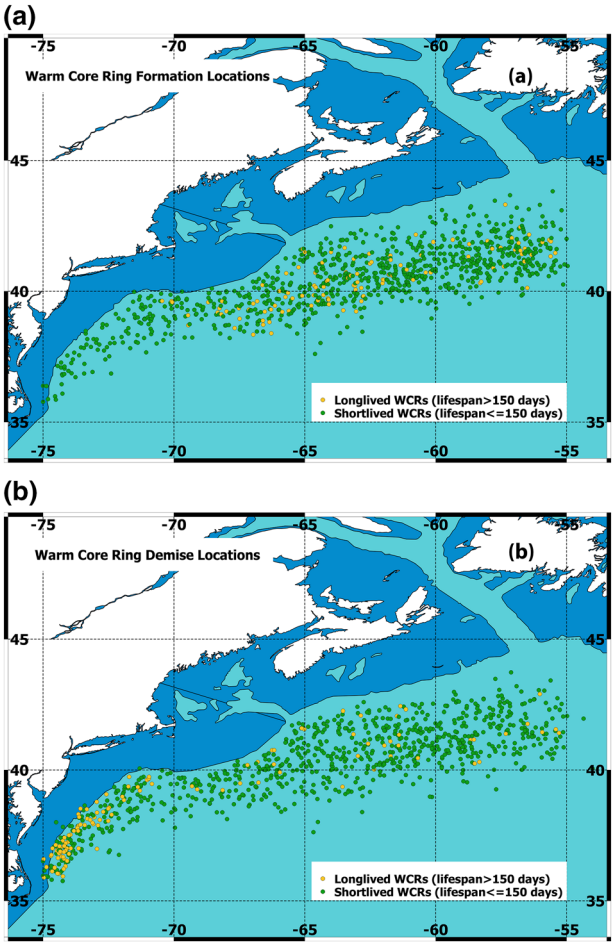

Figure 5. Locations of formation (a) and demise (b) of WCRs when the whole population (1980–2017) is subdivided according to two lifespan groups: <150 days and >150 days of lifespan. Clearly, the longer-living WCRs are formed mostly to the east of 70°W and demise to the west of 70°W.

Similarly, Figure 6d presents the comparison of lifespan of the WCRs formed in each zone between the two regimes. The lifespan of an average WCR has decreased during the recent regime compared to the earlier regime for all zones and seasons, except for Zone 1 in spring and summer, and for Zone 2 in summer (see Figure 6d). In Zone 1, the mean lifespan has increased from 30 to 40 days in spring and from 35 to 45 days in summer. In Zone 2, the mean lifespan for summertime rings has increased from 70 to 90 days.

3.4. Size Characteristics

The size variation of WCRs as a function of their formation longitude has been divided into four size groups of equal bin width: $R < 50$ km, $50\ \text{km} \le R \le 100$ km, $100\ \text{km} \le R < 150$ km, and $R \ge 150$ km, where R is the equivalent radius of the WCR. For elliptical rings, an equivalent "radius" (R) was calculated by equating the area of the ellipse (πab, where a and b are semimajor and semiminor axes) to that of an equivalent circular eddy (πR^2). Each of the size groups were divided using the same 5° binning system we used for investigating the overall geographic distribution from 75°W to 55°W.

The size distribution of WCRs for the whole period (1980–2017) is shown in Figure 7a. The WCRs from the smallest size group ($R < 50$ km) are less abundant in Zone 2 (70–65°W) than any of the other three zones. The next two size groups ($50\ \text{km} \le R < 100$ km and $100\ \text{km} \le \text{R} < 150$ km) are more prevalent east of 65°W. It is interesting that Zones 2, 3, and 4 have a definite preference to generate ring sizes in the 50- to 100-km radius.

4. Discussion

In this section, we discuss some of the major dynamical factors that are identifiable for the observed variability of the WCR characteristics presented above (in terms of the regime shift differences, seasonality, lifespan, and size distribution).

4.1. Regime Shift

Gangopadhyay et al. (2019) hypothesized that the increase of the number of WCR formations since 2000 could be related to increased instability of the GS due to several factors, such as (i) decreasing reduced gravity between the slope and the GS due to warming of the slope (via atmospheric forcing), (ii) internal dynamics of the GS system (including transport, latitudinal movement, and interactions with the Deep Western Boundary Current (DWBC) and NESC, and (iii) changes in the large-scale atmospheric forcing (basin-scale wind stress curl), or a combination of these factors. Further targeted numerical and data-based analysis using recent OOI Pioneer Array and Processes of Exchange At Cape Hatteras (PEACH) (Andres et al., 2020; Gawarkiewicz et al., 2018; Todd, 2020) observations would be necessary to address and understand how changes in important dynamical factors such as the Rossby or Burger numbers relative to past decades could be related to the development of the regime shift.

For example, one important suspect for the cause of the regime shift is the wind stress curl over the subtropical North Atlantic. This generates westward propagating Rossby waves to generate the western boundary current (Dengg, 1996; Gangopadhyay et al., 1992; Gill, 1982; Haidvogel & Beckmann, 1999). Recently, the decadal-scale northward (southward) shifts of the Kuroshio Extension have been shown to be associated with its weak (strong) transport and unstable (stable) meandering configuration (Qiu & Chen, 2010). These opposing phases were linked to the basin-wide wind stress curl forced negative (positive) SSH anomalies propagating west in the form of Rossby waves during negative (positive) phases of the North Pacific Gyre Oscillation. Furthermore, Yang and Liang (2018) recently showed that the strong and stable state of the Kuroshio extension is also associated with a strong southern recirculation gyre. Future studies are needed

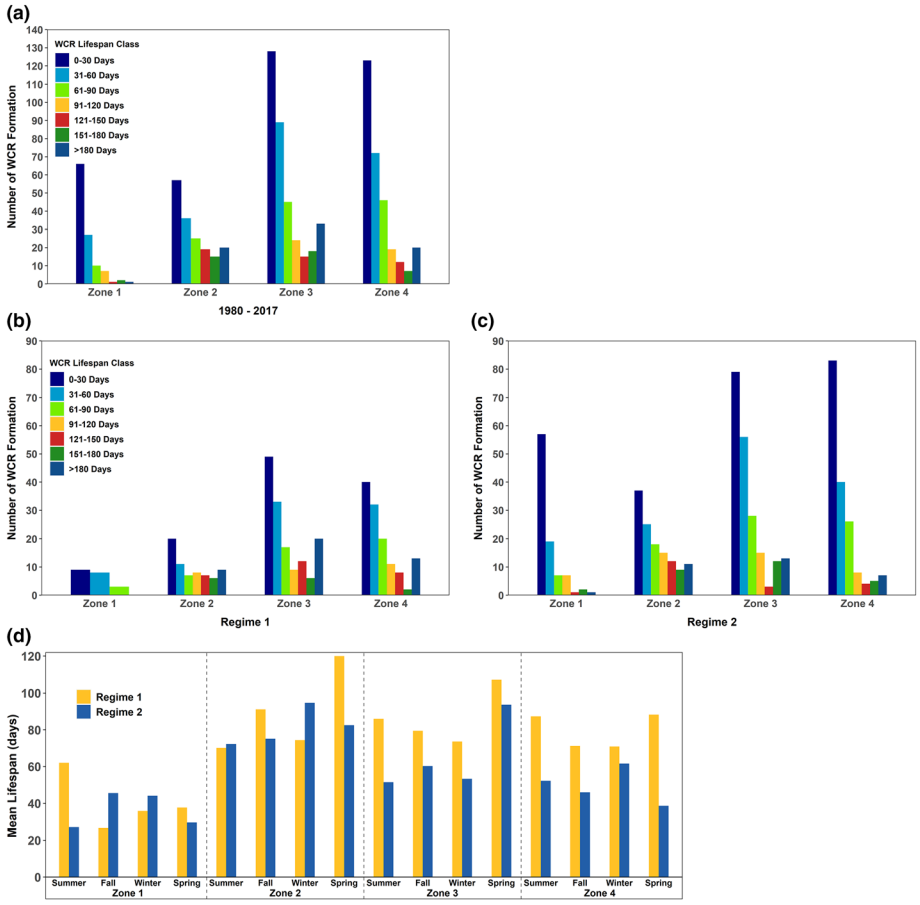

Figure 6. (a) Geographic distribution of WCR lifespan after formation in the zone. (b) is for lifespan distribution for each zone in Regime 1, and (c) is for lifespan distribution in each zone in Regime 2. (d) Seasonal and zone-wise WCR formations across two regimes. The zones are as follows. Zone 1: 75–70°W, Zone 2: 70–65°W, Zone 3: 65–60°W, and Zone 4: 60–55°W.

to investigate the possibility of a weakening southern recirculation gyre during the past two decades that could add to the increasingly unstable state of the GS. Such investigations should also reconcile with recent observations of westward movement of the destabilization point of the GS (Andres, 2016). Below, we highlight some of the dynamical implications of the results presented for the observations of seasonal behavior and changes in WCR attributes (number, lifespan, and size) from Regime 1 to Regime 2 based on the 38-year record.

4.2. Seasonality

This census confirms the previously indicated seasonal cycle of WCR formations with summer peaks and winter lows. This seasonality was prevalent for the whole 75–55°W area, in the four 5° zones, and over the two regimes. The causality of such a seasonal peak can now be examined through baroclinic/barotropic instability mechanisms with advanced numerical modeling experiments.

The WCR formation process has been linked with GS instability processes, which convert the available potential energy to the eddy kinetic energy (EKE) (Gill et al., 1974; Robinson et al., 1988; Stammer, 1998). Previous statistical studies on WCRs have also indicated that the ring production by the GS system peaks during the summer months. Zhai et al. (2008) analyzed satellite altimeter data and found that in the GS area (73–44°W), EKE peaks in summer while the ocean is most baroclinically unstable during the winter. They argued that it is not seasonally varying Ekman pumping but the reduced dissipation of EKE in summer, which is responsible for the EKE seasonal cycle. The reduced dissipation is caused by the thermal capping

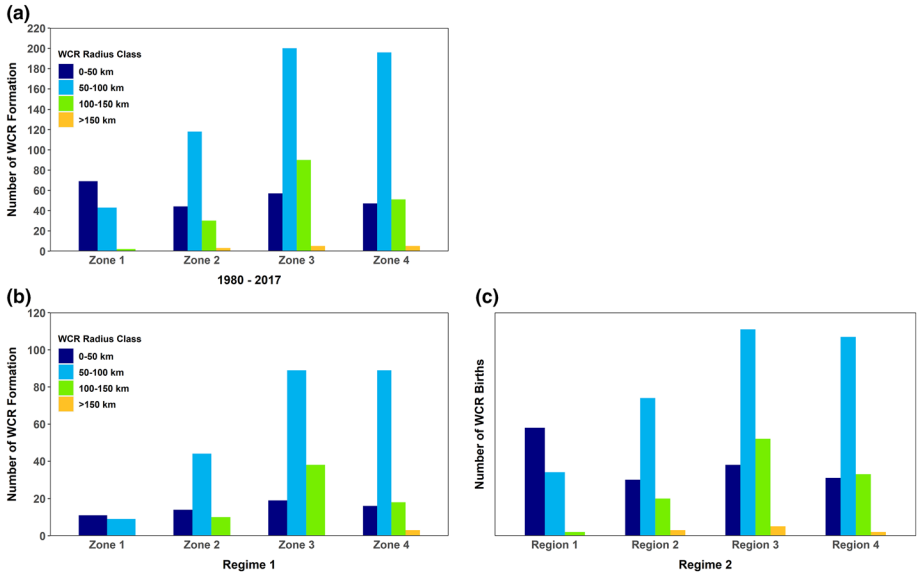

Figure 7. (a) Geographic distribution of WCR size after formation in the zone. Lifespan and Size distribution difference between the two regimes. (b) is for size distribution for each zone in Regime 1, and (c) is for size distribution in each zone in Regime 2. The zones are as follows. Zone 1: 75–70°W, Zone 2: 70–65°W, Zone 3: 65–60°W, and Zone 4: 60–55°W. Regime 1: 1980–1999 and Regime 2: 2000–2017.

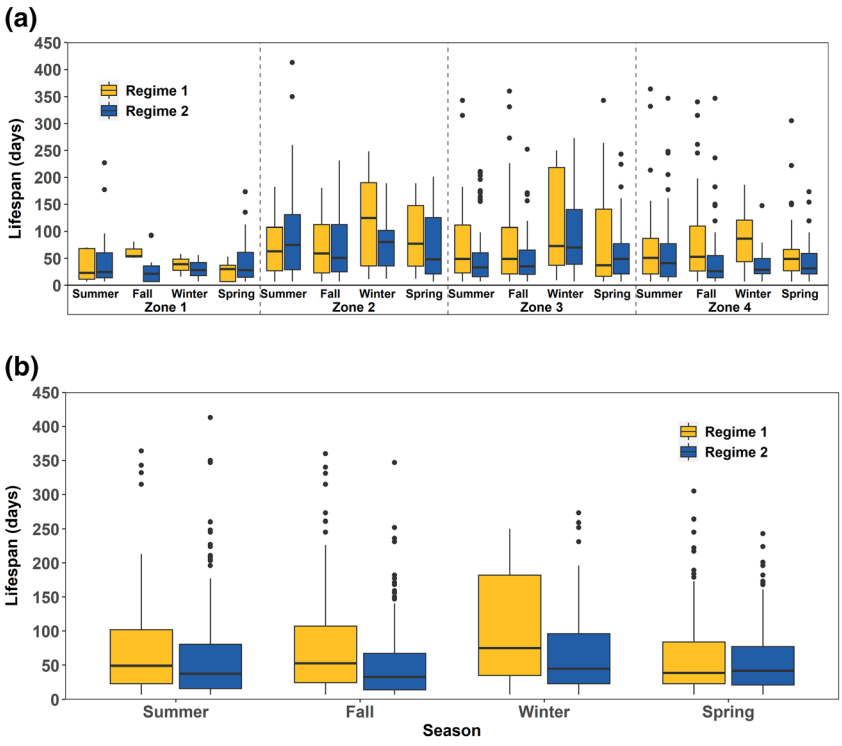

Figure 8. (a) Seasonal and zone-wise lifespan distribution of GS WCRs across regimes. (b) Seasonal lifespan distribution of GS WCR across regimes.

Table 3
Seasonal Variation of WCR Characteristics (Formation Number, Mean Size and Mean Lifespan) for the Four Zones in the Two Different Regimes

		WCR formation number		Mean WCR size (radius, km)		Mean WCR lifespan (days)	
		Regime 1	Regime 2	Regime 1	Regime 2	Regime 1	Regime 2
Zone 1	Summer	5	32	39.98	49.24	35.80	44.13
	Fall	3	24	47.10	48.50	62.00	27.00
	Winter	3	8	53.18	50.22	37.67	29.50
	Spring	9	30	48.97	49.30	26.56	45.50
Zone 2	Summer	19	47	63.41	63.23	74.37	94.62
	Fall	17	34	78.20	91.43	70.12	72.26
	Winter	14	14	77.40	65.15	119.93	82.50
	Spring	18	32	73.14	76.71	91.11	75.13
Zone 3	Summer	56	64	80.51	82.78	73.63	53.33
	Fall	33	52	78.78	88.39	85.97	51.48
	Winter	22	38	80.55	78.64	107.27	93.62
	Spring	35	53	80.17	73.95	79.46	60.21
Zone 4	Summer	37	61	79.06	75.05	70.92	61.61
	Fall	31	47	83.56	74.54	87.32	52.21
	Winter	18	22	78.79	80.36	88.22	38.59
	Spring	40	43	72.14	77.76	71.20	45.95

Note. Zone 1: 75–70°W; Zone 2: 70–65°W; Zone 3: 65–60°W; and Zone 4: 60–55°W. Regime 1: 1980–1999 and Regime 2: 2000–2017.

of the thermocline in the summer; while in the winter, eddies are heavily impacted by thermal interaction with the atmosphere above.

Kang et al. (2016) used a set of three numerical experiments with different surface wind and buoyancy forcing to analyze the mechanisms governing the seasonal cycle of upper ocean energetics. They found that in the GS area (75–55°W) EKE has a dominant peak in May and a secondary peak in September near the surface. Their results also suggest the seasonal cycle of the surface EKE in this area lags the cycle of baroclinic instability by two to three months. However, the September peak of EKE is driven by the wind forcing. A similar correlation between surface EKE and the baroclinic instability was observed in the North Pacific (Qiu, 1999) and the southern Indian Ocean (Jia et al., 2011). In these cases, a theoretical model was used to show that the lag of a couple of months corresponds to the length of time for unstable waves to grow in the respective areas.

Three inferences are apparent from the analysis over the four zones: (i) The summertime WCR formation is almost twice that in the winter for Zones 2, 3, and 4; (ii) the wintertime formation rate is the least in all zones; and (iii) the fall formation is similar to summertime for Zones 1 and 2, while less than summertime formation in Zones 3 and 4.

4.3. Lifespan

The lifespan distribution shows an evolution from a bimodal character obtained in the early periods of 1974–1983 from B86 and of 1980–1983 in this study to an exponential nature in the late 1980s and continuing through the recent decade. The ring formation numbers decay exponentially with an *e*-folding scale of 60–80 days (Figure 4 and section 3.3).

Figure 8b compares the lifespan of the WCRs formed in each of the four zones between the two regimes. Clearly, the lifespan of an average WCR has decreased during the recent regime compared to the earlier regime for all zones and seasons, except for Zone 1 in spring and summer and for Zone 2 in summer (Figure 8b and Table 3). Specifically, in Zone 1, the mean lifespan has increased from 30 to 40 days in spring and from 35 to 45 days in summer. In Zone 2, the mean lifespan for summertime rings has increased from 70 to 90 days.

This anomalous increase in lifespan in the more coastal areas paired with the regime shift, might be a contributing cause of the observed warming of the western shelf area (75–65°W). This was briefly discussed by Gawarkiewicz et al. (2018) and needs further detailed investigation.

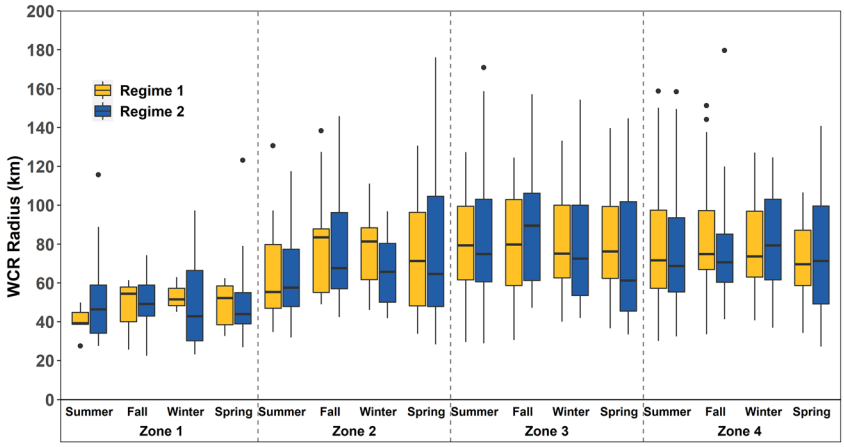

Figure 9. Seasonal and zone-wise size distribution of GS WCRs across regimes.

4.4. Size

The preferred ring size (50–100 km) (Figure 7a) agrees well with the prevalent internal Rossby radius of the GS system. Both Zones 3 and 4 produced a similar number of rings for the largest WCR group ($R \geq 150$ km) and were most productive overall. Interestingly no WCR from this size group was found between 75°W and 70°W indicating the absence of large-amplitude GS meandering and the dominance of a standing meander.

The relative geographic size distribution for each individual regime (Figures 7b and 7c) was also found to be very similar to that for the whole period as shown in Figure 7a with a general increase in number of rings from Regime 1 to Regime 2.

While the mean WCR size over different seasons showed a narrow range of variation in both regimes, the minimum sizes were during spring and maximum during fall, which are indicative of the start of the active season during spring and more mature ring shedding from high-amplitude meandering in fall (Figures 9a and 9b). The wintertime rings lived longer in both regimes, while the generally large number of larger-size fall WCRs had shorter lives during Regime 2.

The size distribution did not change in any statistically significant sense across regimes except in Zone 1. See Figure 9 and Tables 3 and 4 for a comparison of the size distribution between the two regimes. The invariance of the size distribution for Zones 2, 3, and 4 from Regime 1 to Regime 2 indicates that the governing dynamics in determining the sizes is related to topography and large-scale meandering to the east of the NESC. By contrast the lifespan and annual number of ring formations both showed changes temporally, meaning they are likely influenced by other factors such as transport variability and external forcing.

4.5. RFI

The impact of rings is quantified by a RFI, which signifies the presence of a ring and area covered by the rings in a given zone. This index is calculated in two steps. First, the footprint of each individual WCR in each zone

Table 4
Seasonal Variation of WCR Characteristics (Formation Number, Mean Size, and Mean Lifespan) for the Whole Area (75–55°W) in the Two Different Regimes

	WCR formation number		Mean WCR size (radius, km)		Mean WCR lifespan (days)	
Seasons	Regime 1	Regime 2	Regime 1	Regime 2	Regime 1	Regime 2
Summer	117	204	75.5	70.70	71.27	63.87
Fall	84	157	79.3	78.81	82.40	52.46
Winter	57	82	77.8	74.03	100.70	70.42
Spring	102	158	73.0	70.87	73.61	56.56

Note. Regime 1: 1980–1999 and Regime 2: 2000–2017.

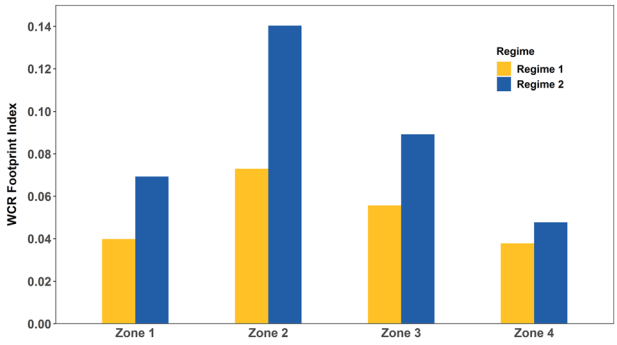

Figure 10. WCR footprint index (RFI) for four zones and two regimes. The order of ring footprint from highest to lowest is Zone 2, Zone 3, Zone 1, and Zone 4, which is similar in both regimes. See text for details.

is obtained using Equation 1. It is important to distinguish between the "age" and "lifespan" of a ring. In Equation 1, the "age" of a ring is the time that has elapsed from its birth to a specific time during the ring's life. "Lifespan" is the maximum "age" that a ring would attain. Note that "a" in Equation 1 is the *expected lifespan* of a ring, which depends on its formation zone and season and events happening during its propagation to the west over its life. The decay rate would depend on its surroundings in the slope, while it encounters the meanders of the Stream, the bathymetry (e.g., the NESC or the shelf break), or another ring. From 38 years of data, we calculated the average lifespan of WCRs formed in a zone for each season. These are presented in in Table 3 and are then used as the expected lifespan (a) in Equation 1 for a ring formed in a particular zone and season to calculate its footprint in all different zones that it transits during its life.

Note that, if a particular ring lived more than its expected lifespan, then the value of "a" was changed to its own lifespan (date of absorption-date of birth, DOA-DOB); otherwise, the decay rate would follow the expected lifespan from Table 3. The exact nature of decay of the size of the rings as they propagate will require a rigorous GIS-based analysis of all the available charts, which is underway. This exercise will quantify all the ring sizes in every chart over 38 years and a systematic statistical analysis on their path, size, decay rate and factors affecting such decay will be carried out in a later study.

Second, the RFI is then calculated using Equation 2 for each zone and each regime and is presented in Figure 10. This normalized index is indicative of the percent area of slope water in a zone that is covered by the WCRs. This first order index might underestimate the actual value due to the definition of the slope water region being bounded by the mean GS northwall and the 200-m isobath in the latitudinal direction and the two relevant longitudes defining the zone itself in the east-west direction.

Two clear inferences can be drawn from Figure 10. First, the maximum impact of the WCRs is on Zone 2 compared to the other zones in both regimes. The RFI varied from highest to lowest in the following order—Zone 2, Zone 3, Zone 1, and Zone 4, which was similar in both regimes. Second, the impact increased in all zones from Regime 1 to Regime 2 with the maximum increase being almost double in Zone 2 (from 7% to more than 14% of the slope area in Zone 2). The GOM and GB regions are directly to the north of Zone 2 and will thus be impacted the most from the regime shift of the WCRs. Such an event was described by Grodsky et al. (2018), who reported the presence of warm and salty surface water in the GOM in the winter of 2017–2018 based on recent satellite observations.

This impact ratio (RFI) can be used as a metric for climatic impacts in the slope waters between the two regimes. The complex interaction of the WCRs with the shelf edge and related interannual variability of the shelf and slope ecosystem can now be quantified more rigorously to identify hot spots along the shelf break following up on limited-period studies such as Bisagni et al. (2019). The RFI can possibly be linked with air/sea temperatures and atmospheric variability (including storms) over the area and eventually to understand ecosystem responses in the future (Chen et al., 2016; Francis & Overland, 2014). This increase in ring presence might have had a considerable impact on the slope and shelf ecosystem in the past two decades, which may guide new research directions.

5. Summary and Conclusions

In this study a 38-year-long (1980–2017) census of WCRs has been developed for a total of 961 rings. A regime shift around 2000 in the WCR formation numbers has been pervasive over all four 5° wide zones within the 75–55°W span of the GS. The WCR formation over the whole area (75–55°W) increased from an average of 18 during Regime 1 (1980–1999) to 33 during Regime 2 (2000–2017). To summarize, the number, lifespan, and size of WCRs generally increase from the western zones to the eastern zones, with more rings being formed east of the NESC, with longer life spans and larger areas. Major results from this study are listed below.

1. Seasonal variability showed late spring and early summer peaking (May-June-July) in WCR formations, while wintertime (January–February) had fewer ring formations. This same seasonal pattern was seen in all four zones.
2. WCR formation numbers in each zone showed a regional variability. Zones 1 and 2 formed 12% and 20% of the total WCRs, respectively, while Zones 3 and 4 produced 68% of the WCRs.
3. Three apparent inferences during both regimes are as follows:
   a. the summer WCR formation is almost twice that in the winter in Zones 2, 3, and 4;
   b. the wintertime formation rate is the least in all zones; and
   c. the fall formations are similar to summertime for Zones 1 and 2 while less than summertime formation in Zones 3 and 4.
4. The formation of WCRs has increased by 46%, 29%, and 27% in Zones 2, 3, and 4, respectively, from Regime 1 to Regime 2. However, in Zone 1 the formation numbers have increased by 79% from Regime 1 to 2 of which summer and fall increments are 84% and 88% respectively.
5. A bimodality observed by B86 in the WCR lifespan structure for the time period 1974–1983 was also observed in our WCR data for the period of 1980–1983. This bimodality was also observed in Regime 2 WCR lifespan structure.
6. WCR lifespan distribution shows a rapid decrease with *e*-folding lifespan of about 90 days.
7. In the seasonal and zone-wise settings, we observed a decrease in WCR mean lifespan from Regime 1 to 2, with the following exceptions. In Zone 1, the mean lifespan has increased from 30 to 40 days in spring and from 35 to 45 days in summer. In Zone 2, the mean lifespan for summertime rings has increased from 70 to 90 days.
8. The 90 days or greater lifespan range is more frequent east of 65°W. The lifespan range 91–120 days is least abundant in Zone 1. Zones 2, 3, and 4 are more productive in forming WCRs with a lifespan of more than 180 days.
9. When size distributions are considered, WCRs with radius, $R < 50$ km were more abundant in Zone 1 than the other three zones. WCRs with radius 50–100 and 100–150 km were formed most frequently in Zones 3 and 4. Zone 2 has a certain preference in generating 50- to 100-km-sized WCRs.
10. No significant difference was observed in WCR size distributions across the two regimes.
11. The RFI varied from highest to lowest following the order—Zone2, Zone 3, Zone 1, and Zone 4 and was similar for both regimes.
12. When the RFI was compared across the two regimes on a subregional scale, it showed an increased in WCR occupancy/presence in each zone from Regime 1 to Regime 2. The increase in Zone 1 was 74%, and in Zone 2 was 92%. In Zones 3 and 4, the RFI increased by around 60% and 26%, respectively.

We highlight some of the immediate applications of the observational results in conclusion. Regional and Global data assimilative models, different ocean-atmosphere coupled and climate simulation models, and various reanalysis products could benefit by quantitative comparisons with the regime shift, seasonality and zonal patterns of WCR formation of the GS system over last four decades. The role of the NESC can now be quantified in targeted modeling experiments to reproduce the results of this observational study. The impact of WCRs in recent years on the observed shelf slope water warming can be studied dynamically as in Zhang and Partida (2018) (and references therein) using this data set. Studies such as Myers and Drinkwater (1989) can be revisited to understand the impact of the larger number of WCRs (after the regime shift in 2000) on the various groundfish populations in the GOM and GB area. In fact, such a high number of WCRs in the slope water might have impacted the ecosystem of the GOM/GB and MAB by making them even warmer and saltier frequently in the first two decades of the 21st century as reported recently by Gawarkiewicz et al. (2019). An investigation for identifying similar regime shift in the recruitment structure of ichthyoplankton and zooplankton is underway. Dong et al. (2019) suggested that the WCRs on the New England continental shelf can contribute to sea level rise through steric effect. Hoarfrost et al. (2019) indicated that the increasing number of WCRs on the continental shelf and slope can impact the rate and nature of organic matter remineralization on the continental shelf. Finally, this WCR census development is a precursor to a similar study for the CCRs shed from the GS on the Sargasso side over a similar 40-year period.

Data Availability Statement

The WCR data from Jenifer Clark (coauthor) and Roger Pettipas were used to develop the original census. All of the WCR census data are available (special thanks to Ms. Nancy Copley) through the auspices of the Biological and Chemical Oceanography Data Management Office (https://www.bco-dmo.org/dataset/810182). We thank the Editor and the reviewers for their thoughtful comments, which have certainly improved the presentation of this manuscript.

Acknowledgments

The authors acknowledge financial support from NOAA (NA11NOS0120038), NSF (OCE-0815679 and OCE-1851242), and SMAST and UMass Dartmouth. G. G. was supported by NSF under Grant OCE-1657853 as well as a Senior Scientist Chair from WHOI. We have benefitted from many discussions on Gulf Stream and WCR with Magdalena Andres, Andre Schmidt, Paula Fratantoni, Jon Hare, Wendell Brown, Kathy Donohue, Tom Rossby, Peter Cornillon, and Randy Watts.

References

Andres, M. (2016). On the recent destabilization of the Gulf Stream path downstream of Cape Hatteras. *Geophysical Research Letters*, *43*, 9836–9842. https://doi.org/10.1002/2016GL069966

Andres, M., Donohue, K. A., Toole, J. M. (2020). The Gulf Stream's path and time-averaged velocity structure and transport at 68.5°W and 70.3°W. *Deep Sea Research Part I: Oceanographic Research Papers*, *156*, 103179. http://doi.org/10.1016/j.dsr.2019.103179

Auer, S. J. (1987). Five-year climatological survey of the Gulf Stream system and its associated rings. *Journal of Geophysical Research*, *92*(C11), 11,709–11,726. https://doi.org/10.1029/JC092iC11p11709

Bisagni, J. (1983). Lagrangian current measurements within the eastern margin of a warm-core Gulf Stream ring. *Journal of Physical Oceanography*, *13*(4), 709–715. https://doi.org/10.1175/1520-0485(1983)013<0709:LCMWTE>2.0.CO;2

Bisagni, J. J. (1976). *Passage of anticyclonic Gulf Stream eddies through Deepwater Dumpsite 106 during 1974 and 1975* (Vol. 76, 1 ed.). Rockville, MD: US Department of Commerce, NOAA, National Marine Fisheries Service.

Bisagni, J. J., Gangopadhyay, A., & Sanchez-Franks, A. (2017). Secular change and inter-annual variability of the Gulf Stream position, 1993–2013, 70°−55°W. *Deep Sea Research Part I: Oceanographic Research Papers*, *125*, 1–10. https://doi.org/10.1016/j.dsr.2017.04.001

Bisagni, J. J., Nichols, O. C., & Pettipas, R. (2019). Interannual variability of Gulf Stream warm-core ring interactions with the outer continental shelf and potential broad scale relationships with longfin squid (Doryteuthis pealeii) relative abundance, 1981–2004. *ICES Journal of Marine Science*, *76*(5), 1257–1270. https://doi.org/10.1093/icesjms/fsz144

Brown, O. B., Cornillon, P. C., Emmerson, S. R., & Carle, H. M. (1986). Gulf Stream warm rings: A statistical study of their behavior. *Deep Sea Research Part A. Oceanographic Research Papers*, *33*(11–12), 1459–1473. https://doi.org/10.1016/0198-0149(86)90062-2

Cerone, J. F. (1984). Satellite observed climatology of warm core Gulf Stream rings and discussion of their possible biological effects (MS thesis). University of Rhode Island.

Chaudhuri, A. H., Bisagni, J. J., & Gangopadhyay, A. (2009). Shelf water entrainment by Gulf Stream warm-core rings between 75°W and 50°W during 1978–1999. *Continental Shelf Research*, *29*(2), 393–406. https://doi.org/10.1016/j.csr.2008.10.001

Chaudhuri, A. H., Gangopadhyay, A., & Bisagni, J. J. (2009). Interannual variability of Gulf Stream warm-core rings in response to the North Atlantic Oscillation. *Continental Shelf Research*, *29*(7), 856–869. https://doi.org/10.1016/j.csr.2009.01.008

Chen, K., Gawarkiewicz, G. G., Lentz, S. J., & Bane, J. M. (2014). Diagnosing the warming of the Northeastern US Coastal Ocean in 2012: A linkage between the atmospheric jet stream variability and ocean response. *Journal of Geophysical Research: Oceans*, *119*, 218–227. https://doi.org/10.1002/2013JC009393

Chen, K., Kwon, Y., & Gawarkiewicz, G. (2016). Interannual variability of winter-spring temperature in the Middle Atlantic Bight: Relative contributions of atmospheric and oceanic processes. *Journal of Geophysical Research: Oceans*, *121*, 4209–4227. https://doi.org/10.1002/2016JC011646

Cornillon, P. (1986). The effect of the New England Seamounts on Gulf Stream meandering as observed from satellite IR imagery. *Journal of Physical Oceanography*, *16*(2), 386–389. https://doi.org/10.1175/1520-0485(1986)016<0386:TEOTNE>2.0.CO;2

Csanady, G. (1979). The birth and death of a warm core ring. *Journal of Geophysical Research*, *84*(C2), 777–780. https://doi.org/10.1029/JC084iC02p00777

Decker, B. L. (1986). *World Geodetic System 1984.* Afs, Missouri: Defense Mapping Agency Aerospace Center St Louis.

Dengg, J. (1996). The gulf stream separation problem. *The Warmwatersphere of the North Atlantic Ocean*, 254–290.

Dong, S., Baringer, M. O., & Goni, G. J. (2019). Slow down of the Gulf Stream during 1993–2016. *Scientific Reports*, *9*(1), 6672.

Flierl, G. R. (1977). The application of linear quasigeostrophic dynamics to Gulf Stream rings. *Journal of Physical Oceanography*, *7*(3), 365–379. https://doi.org/10.1175/1520-0485(1977)007<0365:TAOLQD>2.0.CO;2

Francis, J. A., & Overland, J. E. (2014). *Implications of rapid Arctic change for weather patterns in northern mid-latitudes* 12(3), 10–13. Washington DC: US CLIVAR Variations.

Gangopadhyay, A., Chaudhuri, A. H., & Taylor, A. H. (2016). On the nature of temporal variability of the Gulf Stream path from 75° to 55°W. *Earth Interactions*, *20*(9), 1–17. https://doi.org/10.1175/EI-D-15-0025.1

Gangopadhyay, A., Cornillon, P., & Watts, D. R. (1992). A test of the Parsons–Veronis hypothesis on the separation of the Gulf Stream. *Journal of Physical Oceanography*, *22*(11), 1286–1301. https://doi.org/10.1175/1520-0485(1992)022<1286:atotph>2.0.co;2

Gangopadhyay, A., & Gawarkiewicz, G. (2020). Yearly census of Gulf Stream Warm Core Ring formation from 1980 to 2017. Biological and chemical oceanography data management office (BCO-DMO). Dataset version 2020-05-06. https://doi.org/10.26008/1912/bco-dmo.810182.1

Gangopadhyay, A., Gawarkiewicz, G., Silva, E. N. S., Monim, M., & Clark, J. (2019). An observed regime shift in the formation of warm core rings from the Gulf Stream. *Scientific Reports*, *9*(1), 12319. https://doi.org/10.1038/s41598-019-48661-9

Gangopadhyay, A., Schmidt, A., Agel, L., Schofield, O., & Clark, J. (2013). Multiscale forecasting in the western North Atlantic: Sensitivity of model forecast skill to glider data assimilation. *Continental Shelf Research*, *63*, S159–S176. https://doi.org/10.1016/j.csr.2012.09.013

Gawarkiewicz, G., Bahr, F., Beardsley, R. C., & Brink, K. H. (2001). Interaction of a slope eddy with the shelfbreak front in the Middle Atlantic Bight. *Journal of Physical Oceanography*, *31*(9), 2783–2796. https://doi.org/10.1175/1520-0485(2001)031<2783:IOASEW>2.0.CO;2

Gawarkiewicz, G., Chen, K., Forsyth, J., Bahr, F., Mercer, A. M., Ellertson, A., et al. (2019). An advective marine heatwave in the Middle Atlantic Bight: Shelfbreak exchange driven thermohaline anomalies in early 2017. *Frontiers in Marine Science*, *6*, 712. https://doi.org/10.3389/fmars.2019.00712

Gawarkiewicz, G., & Plueddemann, A. J. (2020). Scientific rationale and conceptual design of a process-oriented shelfbreak observatory: The OOI Pioneer Array. *Journal of Operational Oceanography*, *13*(1), 19–36. https://doi.org/10.1080/1755876x.2019.1679609

Gawarkiewicz, G., Todd, R. E., Zhang, W., Partida, J., Gangopadhyay, A., Monim, M., et al. (2018). The changing nature of shelf-break exchange revealed by the OOI Pioneer Array. *Oceanography*, *31*(1), 60–70. https://doi.org/10.5670/oceanog.2018.110

Gill, A. E. (1982). *Atmosphere-ocean dynamics*, *International Geophysics Series*, London, UK: Academic Press.

Gill, A., Green, J., & Simmons, A. (1974). Energy partition in the large-scale ocean circulation and the production of mid-ocean eddies. *Deep Sea Research*, *21*(7), 499–528.

Grodsky, S. A., Vandemark, D., Feng, H., & Levin, J. (2018). Satellite detection of an unusual intrusion of salty slope water into a marginal sea: Using SMAP to monitor Gulf of Maine inflows. *Remote Sensing of Environment*, *217*, 550–561. https://doi.org/10.1016/j.rse.2018.09.004

Hackeloeer, A., Klasing, K., Krisp, J. M., & Meng, L. (2014). Georeferencing: A review of methods and applications. *Annals of GIS*, *20*(1), 61–69. https://doi.org/10.1080/19475683.2013.868826

Haidvogel, D. B., & Beckmann, A. (1999). *Numerical ocean circulation modeling*.

Halliwell, G. R., & Mooers, C. N. (1979). The space-time structure and variability of the shelf water-slope water and Gulf Stream surface temperature fronts and associated warm-core eddies. *Journal of Geophysical Research*, *84*(C12), 7707–7725. https://doi.org/10.1029/JC084iC12p07707

Hamilton, J. D., & Susmel, R. (1994). Autoregressive conditional heteroskedasticity and changes in regime. *Journal of Econometrics*, *64*(1–2), 307–333. https://doi.org/10.1016/0304-4076(94)90067-1

Hoarfrost, A., Balmonte, J. P., Ghobrial, S., Ziervogel, K., Bane, J., Gawarkiewicz, G., & Arnosti, C. (2019). Gulf Stream ring water intrusion on the Mid-Atlantic Bight continental shelf break affects microbially-driven carbon cycling. *Frontiers in Marine Science*, *6*, 394. https://doi.org/10.3389/fmars.2019.00394

Jia, F., Wu, L., & Qiu, B. (2011). Seasonal modulation of eddy kinetic energy and its formation mechanism in the Southeast Indian Ocean. *Journal of Physical Oceanography*, *41*(4), 657–665. https://doi.org/10.1175/2010JPO4436.1

Joyce, T., & Wiebe, P. (1983). Warm-core rings of the Gulf-Stream. *Oceanus*, *26*(2), 34–44.

Joyce, T. M. (1985). Gulf Stream warm-core ring collection: An introduction. *Journal of Geophysical Research*, *90*(C5), 8801–8802. https://doi.org/10.1029/JC090iC05p08801

Joyce, T. M., & McDougall, T. J. (1992). Physical structure and temporal evolution of Gulf Stream warm-core ring 82B. *Deep Sea Research Part A. Oceanographic Research Papers*, *39*, S19–S44. https://doi.org/10.1016/S0198-0149(11)80003-8

Kang, D., Curchitser, E. N., & Rosati, A. (2016). Seasonal variability of the Gulf Stream kinetic energy. *Journal of Physical Oceanography*, *46*(4), 1189–1207. https://doi.org/10.1175/JPO-D-15-0235.1

Kim, C., & Nelson, C. R. (1999). *State-space models with regime switching: Classical and Gibbs-sampling approaches with applications*. Cambridge, MA: The MIT press.

Lai, D. Y., & Richardson, P. L. (1977). Distribution and movement of Gulf Stream rings. *Journal of Physical Oceanography*, *7*(5), 670–683. https://doi.org/10.1175/1520-0485(1977)007<0670:DAMOGS>2.0.CO;2

Lee, T., & Cornillon, P. (1996). Propagation and growth of Gulf Stream meanders between 75 and 45°W. *Journal of Physical Oceanography*, *26*(2), 225–241. https://doi.org/10.1175/1520-0485(1996)026<0225:PAGOGS>2.0.CO;2

Monim, M. (2017). Seasonal and inter-annual variability of Gulf Stream Warm Core Rings from 2000 to 2016. [e-version] MS. University of Massachusetts Dartmouth.

Myers, R. A. & Drinkwater, K. (1986). The effects of entrainment of shelf water by warm core rings on Northwest Atlantic fish recruitment. ICES CM, 100, pp.13.

Myers, R. A., & Drinkwater, K. (1989). The influence of Gulf Stream warm core rings on recruitment of fish in the northwest Atlantic. *Journal of Marine Research*, *47*(3), 635–656. https://doi.org/10.1357/002224089785076208

Olson, D., Schmitt, R., Kennelly, M., & Joyce, T. (1985). A two-layer diagnostic model of the long-term physical evolution of warm-core ring 82B. *Journal of Geophysical Research*, *90*(C5), 8813–8822. https://doi.org/10.1029/JC090iC05p08813

Perlin, M. (2014). MS_Regress–The MATLAB package for Markov regime switching models. 2012. *Available at SSRN*

QGIS Development team, (2016). QGIS Geographic Information System[e-]. 2.18.16 ed. Open Source Geospatial Foundation. <http://qgis.org>.

QGIS Project, (2016). Vector calculator. [on-line] available at: <https://docs.qgis.org/2.18/en/docs/training_manual/processing/vector_calculator.html?highlight=calculator> [accessed: 01/30 2019].

Qiu, B. (1999). Seasonal eddy field modulation of the North Pacific Subtropical Countercurrent: TOPEX/Poseidon observations and theory. *Journal of Physical Oceanography*, *29*(10), 2471–2486. https://doi.org/10.1175/1520-0485(1999)029<2471:SEFMOT>2.0.CO;2

Qiu, B., & Chen, S. (2010). Eddy-mean flow interaction in the decadally modulating Kuroshio Extension system. *Deep Sea Research Part II: Topical Studies in Oceanography*, *57*(13–14), 1098–1110. https://doi.org/10.1016/j.dsr2.2008.11.036

Ramp, S., Beardsley, R., & Legeckis, R. (1983). An observation of frontal wave development on a shelf-slope/warm core ring front near the shelf break south of New England. *Journal of Physical Oceanography*, *13*(5), 907–912. https://doi.org/10.1175/1520-0485(1983)013<0907:AOOFWD>2.0.CO;2

Richardson, P. (1983). *Gulf Stream rings. 1983. Eddies in marine science*. (pp. 19–45). Berlin, Heidelberg: Springer. https://doi.org/10.1007/978-3-642-69003-7_2

Robinson, A. R., Spall, M. A., & Pinardi, N. (1988). Gulf Stream simulations and the dynamics of ring and meander processes. *Journal of Physical Oceanography*, *18*(12), 1811–1854. https://doi.org/10.1175/1520-0485(1988)018<1811:GSSATD>2.0.CO;2

Rodionov, S. N. (2004). A sequential algorithm for testing climate regime shifts. *Geophysical Research Letters*, *31*, L09204. https://doi.org/10.1029/2004GL019448

Rodionov, S. N. (2006). Use of prewhitening in climate regime shift detection. *Geophysical Research Letters*, *33*, L12707. https://doi.org/10.1029/2006GL025904

Rodionov, S. N., & Overland, J. E. (2005). Application of a sequential regime shift detection method to the Bering Sea ecosystem. *ICES Journal of Marine Science*, *62*(3), 328–332. https://doi.org/10.1016/j.icesjms.2005.01.013

Saunders, P. M. (Ed) (1971). *Deep Sea Research and Oceanographic Abstracts*. New York, NY: Elsevier.

Schmidt, A., & Gangopadhyay, A. (2013). An operational ocean circulation prediction system for the western North Atlantic: Hindcasting during July–September of 2006. *Continental Shelf Research*, *63*, S177–S192. https://doi.org/10.1016/j.csr.2012.08.017

Schofield, O., Glenn, S., Orcutt, J., Arrott, M., Meisinger, M., Gangopadhyay, A., et al. (2010). Automated sensor network to advance ocean science. *Eos, Transactions American Geophysical Union*, *91*(39), 345–346. https://doi.org/10.1029/2010EO390001

Silva, E. N. S. (2019). Understanding thirty-eight years of Gulf Stream's warm core rings: Variability, regimes and survival. *MS Thesis*, University of Massachusetts Dartmouth, 125 pp.

Stammer, D. (1998). On eddy characteristics, eddy transports, and mean flow properties. *Journal of Physical Oceanography*, *28*(4), 727–739. https://doi.org/10.1175/1520-0485(1998)028<0727:OECETA>2.0.CO;2

Todd, R. E. (2020). Export of middle Atlantic Bight Shelf waters near Cape Hatteras from two years of underwater glider observations. *Journal of Geophysical Research: Oceans*, *125*(4). https://doi.org/10.1029/2019jc016006

Yang, Y., & San Liang, X. (2018). On the seasonal eddy variability in the Kuroshio Extension. *Journal of Physical Oceanography*, *48*(8), 1675–1689. https://doi.org/10.1175/JPO-D-18-0058.1

Zhai, X., Greatbatch, R. J., & Kohlmann, J. (2008). On the seasonal variability of eddy kinetic energy in the Gulf Stream region. *Geophysical Research Letters*, *35*, L24609. https://doi.org/10.1029/2008GL036412

Zhang, W. G., & Gawarkiewicz, G. G. (2015). Dynamics of the direct intrusion of Gulf Stream ring water onto the Mid-Atlantic Bight shelf. *Geophysical Research Letters*, *42*, 7687–7695. https://doi.org/10.1002/2015GL065530

Zhang, W. G., & Partida, J. (2018). Frontal subduction of the Mid-Atlantic Bight shelf water at the onshore edge of a warm-core ring. *Journal of Geophysical Research: Oceans*, *123*, 7795–7818. https://doi.org/10.1029/2018JC013794